8 S. Irmay, On the theoretical derivation of Darcy and Forchheimer formulas, *Trans. Amer. Geophys. Union* 39, No. 4 (1958).
9 Y. C. Pao, E. L. Ritman, and E. H. Wood, Finite element analysis of left ventricular myocardial stresses, *J. Biomech.* 7:469–477 (1974).
10 G. Paria, Flow of fluids through porous deformable solids, *Applied Mechanics Survey*, Spartem Books, 1972, pp. 901–907.
11 S. Sorek, A stationary principle for nonconservative systems, *Adv. Water Res.* 7:85–88 (1984).

6-B
#6

A Porous-Medium Approach for Modeling Heart Mechanics. II. 1-D Case

SHAUL SOREK AND SAMUEL SIDEMAN
Department of Biomedical Engineering, Technion, Haifa 32000, Israel

Received 7 November 1985; revised 20 March 1986

ABSTRACT

A porous-medium approach is used for modeling mechanics of the left ventricle (LV) of the heart. As a first approximation, a one-dimensional configuration is adopted. Motion of the endocardium and epicardium is formulated explicitly as a periodic function of time, and the mass and momentum balance equations are solved analytically. Detailed blood pressure and velocity profiles in the LV cavity are obtained. Separate expressions are derived for the fluid pressure in the myocardium, the relative fluid-solid velocity, and the stress distribution in the solid portion of the wall.

INTRODUCTION

A one-dimensional model for simulating the mechanics of the left ventricle is presented. The derivation of the pressure, velocity, and stress distributions is based on a porous-medium approach both for the cavity and for the myocardium, as described by the authors in paper I [9], where the advantages of this method in handling complex phenomena in space and time as a continuum are also described. One-dimensional analysis of the myocardium is rather common, and can be justified formally by the low ratio of the wall thickness to the diameter of the LV, as well as by the uniformity of the muscle characteristics over it; an additional point in its favor is the fact that the cross-myocardium direction is the most important one. The rationale for modeling the ellipsoid-shaped cavity by a cylindrical configuration consists in the assumption that the main fluid motion takes place in the core of the cavity, where the blood moves with minimum friction as a plug (or piston) in each beat. In spite of its restrictive simplicity, the one-dimensional model permits qualitative assessment and quantitative evaluation of certain phenomena, and yields (at least as a first approximation) physical relationships and simplified descriptions of the biophysiological functions. At the present stage, the mechanics is evaluated on the basis of phasic physiological measurements of specific fluxes and pressures at the

©Elsevier Science Publishing Co., Inc., 1986

boundaries of the LV (the aortic valve) and the epicardium (the intake to the coronary tree). A periodic transfer function for the endocardial and epicardial movements is adopted on the basis of actual physiological measurements of the maximum displacements of the endocardium and epicardium. Such a function reflects implicitly the independent biomechanical activation of the muscle contractions over the cycle, and its second time derivative will serve as the inertial term in the driving force controlling the stress gradient in the tissue. This approach dispenses with the classical stress-strain relation in describing the wall motion, at the same time permitting a closed-form solution and an analytical expression for the phase difference between the endocardial and epicardial displacements.

MATHEMATICAL MODEL FOR 1-D CONFIGURATION

Consider the LV as a straight, long and narrow cylindrical tube. The myocardium is represented by a flexible sponge between two impermeable plates with inflow and outflow taking place through the coronary vessel (see Figure 1).

Let V_T denote the total volume of the tube, V_{SB} the mean solid volume of compartment B, and V_{TB} the time dependent total volume of B, defined as

$$V_{TB} = V_T - Ax_1 = V_T\left(1 - \frac{x_1}{L}\right), \tag{1}$$

where L is the length of the tube, A the area of its cross section, and x_1 the displacement of the endocardium, given by

$$x_1 = \bar{x}_1 + \hat{x}_1 \sin \omega t \tag{2}$$

with ω the average cardiac beat frequency ($= 2\pi/$cycle time). The porosity

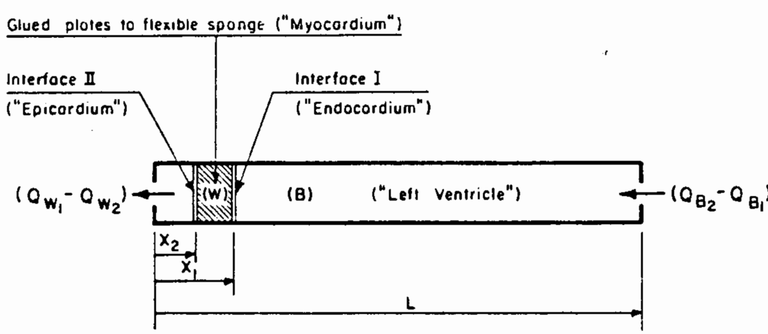

FIG. 1. 1-D simulation of the left ventricle.

n_B in the chamber B is defined as

$$n_B = \frac{V_{TB} - V_{SB}}{V_{TB}}. \tag{3}$$

By virtue of Equations (1) and (3), we may write

$$n_B = 1 - \eta_B, \tag{4}$$

where

$$\eta_B = \frac{\eta_0}{1 - x_1/L}; \qquad \eta_0 = \frac{V_{SB}}{V_T}. \tag{5}$$

Local spatial averaging, using a backward difference for time approximation, leads to a momentum balance equation for the blood in the LV, in the form

$$(aq_B^* + b^*)\, q_B^* \cong -\frac{\partial \psi_B}{\partial x} + d^*, \tag{6}$$

where

$$a = \frac{\eta_B}{gV_{sB}}\left(\frac{1}{1 - \eta_B}\right)^3, \tag{7.1}$$

$$b^* = a\frac{\nu}{V_{sB}}\eta_B\left[1 + \frac{V_{sB}^2}{\nu \Delta t}\left(\frac{1 - \eta_B}{\eta_B}\right)^2\right], \tag{7.2}$$

$$d^* = \frac{1}{g}\frac{q_B^k}{\Delta t}\left(\frac{1}{1 - \eta_B}\right). \tag{7.3}$$

Here, ψ_B is the pressure head at the LV; g the acceleration of gravity; ν the kinematic viscosity of the blood; and $\Delta t = t^{k+1} - t^k$ the time step between two consecutive time levels, $(\ )^k$ denoting the value at the preceding time level. Thus is view of Equations (6), (7), we obtain

$$q_B^* = n_B v_B = -Z\frac{\partial \psi_B^*}{\partial x}, \tag{8}$$

where $Z = Z(\partial \psi_B/\partial x)$, the permeability function, is given by

$$Z = \left[\frac{b^*}{2} + \sqrt{\left(\frac{b^*}{2}\right)^2 + a\left|d^* - \frac{\partial \psi_B}{\partial x}\right|}\,\right]^{-1}, \tag{9}$$

and v_B is the instantaneous velocity of the blood.

Mass continuity for a fluid without sources or sinks dictates

$$\frac{\partial n_B}{\partial t} + \frac{\partial}{\partial x}(n_B v_B) = 0. \tag{10}$$

In view of Equations (2)–(5) and (8)–(10), we obtain a flow equation of the form

$$-\eta_0 \frac{\mathring{x}_1}{L} \omega \frac{\cos \omega t}{(1 - x_1/L)^2} = Z \frac{\partial^2 \psi_B^*}{\partial x^2}. \tag{11}$$

Equation (11) is to be stored for ψ_B^*, subject to

$$\psi_B^* = \psi_{B_L} \qquad t \geqslant 0, \quad x = L, \tag{12.1}$$

$$-Z\frac{\partial \psi_B^*}{\partial x} = Q_{B2} - Q_{B1} \qquad t \geqslant 0, \quad x = L, \tag{12.2}$$

where $Q_{B2} - Q_{B1}$ is the resultant inflow-outflow specific flux at the chamber boundary.

Solution of Equations (11)–(12) yields

$$\psi_B^* = \frac{\lambda \varphi}{Z} \frac{(L-x)^2}{2} + \frac{Q_{B2} - Q_{B1}}{Z}(L - x) + \psi_{B_L}, \qquad x_1 \leqslant x \leqslant L, \tag{13}$$

where

$$\lambda = \eta_0 \frac{\mathring{x}_1}{L} \omega, \tag{14.1}$$

$$\varphi = \frac{\cos \omega t}{(1 - x_1/L)^2}. \tag{14.2}$$

It should also be noted that the term $\partial \psi_B / \partial x$ incorporated in Z [Equation (9)] is known from the preceeding iteration. By Equations (8), (13)–(14), the specific flux distribution is given by

$$q_B^* = \lambda \varphi (L - x) + (Q_{B2} - Q_{B1}), \qquad x_1 \leqslant x \leqslant L. \tag{15}$$

Accordingly, closed-form solutions for the pressure head and specific flux, as function of position in LV and of time, were established. Displacement of interface I, the endocardium, was defined *a priori* by its relation to x_1, namely, $H_1(x,t) = x_1$. This allows an analytical solution for the stress distribution in the myocardium, dispensing with stress-strain constitutive laws and strain-displacement compatible laws.

We now define x_2 as the position of the epicardium at interface II, by

$$x_2 = \bar{x}_2 + \mathring{x}_2 \sin(\omega t + \phi) \tag{16}$$

where ϕ is the phase difference between x_2 and x_1. In view of Eqs. (2) and (16), the total wall volume, V_{Tw}, is thus

$$V_{Tw} = A(x_1 - x_2) = A[\bar{x}_1 - \bar{x}_2 + x_0 \sin(\omega t - \xi)], \tag{17}$$

where

$$x_0 = \sqrt{\mathring{x}_1^2 - 2x_1 \mathring{x}_2 \cos \phi + \mathring{x}_2^2}, \tag{18.1}$$

$$\xi = \arctan\left[\frac{\mathring{x}_2 \sin \phi}{\mathring{x}_1 - \mathring{x}_2 \cos \phi}\right]. \tag{18.2}$$

Denoting the mean solid volume of the wall by V_{sw}, the wall porosity n_w is

$$n_w = \frac{V_{Tw} - V_{sw}}{V_{Tw}}, \tag{19}$$

or by Equation (17) and (19)

$$n_w = 1 - \eta_w, \tag{20}$$

where

$$\eta_w = \frac{\bar{\eta}_0}{x_1 - x_2}, \tag{21.1}$$

$$\bar{\eta}_0 = \frac{V_{sw}}{A}. \tag{21.2}$$

Conservation of mass for the fluid and solid portions, without sources or sinks, is expressed respectively by

$$\frac{\partial n_w}{\partial t} + (1 - n_w)\frac{\partial q_w}{\partial x} = 0 \qquad [n_w \neq n_w(x)], \tag{22}$$

$$\frac{\partial q_w}{\partial x} + \frac{\partial v^s}{\partial x} = 0, \tag{23}$$

where q_w is the relative specific flux between the fluid velocity v^F, and the solid velocity v^s given by

$$q_w = n_w(v^F - v^s). \tag{24}$$

With the mass coupling factor, body forces, and the inertial term neglected, the fluid motion equation yields

$$q_w = -K\frac{\partial}{\partial x}(n_w \psi_w), \tag{25}$$

where K, the wall permeability, is

$$K = \gamma^F \frac{n_w}{R}, \tag{26}$$

γ^F being the specific weight of the fluid and R the resistivity to flow, defined by

$$R = \frac{t}{x_1 - x_2}. \tag{27}$$

By virtue of Equations (13) and (28)–(30), we obtain

$$\frac{\partial^2 \psi_w}{\partial x^2} = A_0 \bar{\varphi}, \tag{28}$$

where

$$A_0 = x_0 \frac{\omega}{\gamma^F}, \tag{29.1}$$

$$\bar{\varphi} = R(x_1 - x_2) \frac{\cos(\omega t - \xi)}{(x_1 - x_2 - \bar{\eta}_0)^2}. \tag{29.2}$$

Equation (28) is to be solved for ψ_w subject to

$$\psi_w = \psi^*_{B1}, \qquad x = x_1, \quad t \geqslant 0 \tag{30.1}$$

$$-K \frac{\partial}{\partial x}(n_w \psi_w) = Q_{w1} - Q_{w2}, x = x_2, \quad t \geqslant 0, \tag{30.2}$$

where $Q_{w1} - Q_{w2}$ is the resultant specific flux at the boundary. By virtue of Equations (13) and (28)–(30), we obtain

$$\psi_w = A_1 \frac{x^2}{2} - A_2 x + A_3 \frac{x_1^2}{2} - A_4 x_1 + A_5, \qquad x_2 \leqslant x \leqslant x_1, \tag{31}$$

where

$$A_1 = A_0 \bar{\varphi}, \tag{32.1}$$

$$A_2 = A_1 x_2 + \frac{Q_{w1} - Q_{w2}}{K}, \tag{32.2}$$

$$A_3 = \frac{\lambda\varphi}{Z} - A_1, \tag{32.3}$$

$$A_4 = \frac{1}{Z}(\lambda\varphi L + Q_{B2} - Q_{B1}) - A_2, \tag{32.4}$$

$\lambda\varphi \; L^2 \quad Q_{B2} - Q_{B1}$

By virtue of Equations (23), (25), and (31)–(32) we obtain

$$\frac{\partial v^s}{\partial x} = -\dot{\eta}_w / \eta_w \tag{33}$$

the dot denoting differentiation with respect to time $(\dot{\ }) \equiv d/dt, (\ddot{\ }) \equiv d^2/dt^2$, etc.). Equation (33) is solved subject to

$$v^s = \dot{x}_1; \qquad x = x_1 \quad t \geqslant 0 \tag{34}$$

In view of Equations (33) and (34) we obtain

$$v^2 = \frac{\dot{\eta}_w}{\eta_w}(x_1 - x) + \dot{x}_1 \tag{35}$$

Equation (35) can now be solved for the displacement of the solid, u^s, subject to

$$u^s = x_1; \qquad x = x_1 \quad t > 0 \tag{36}$$

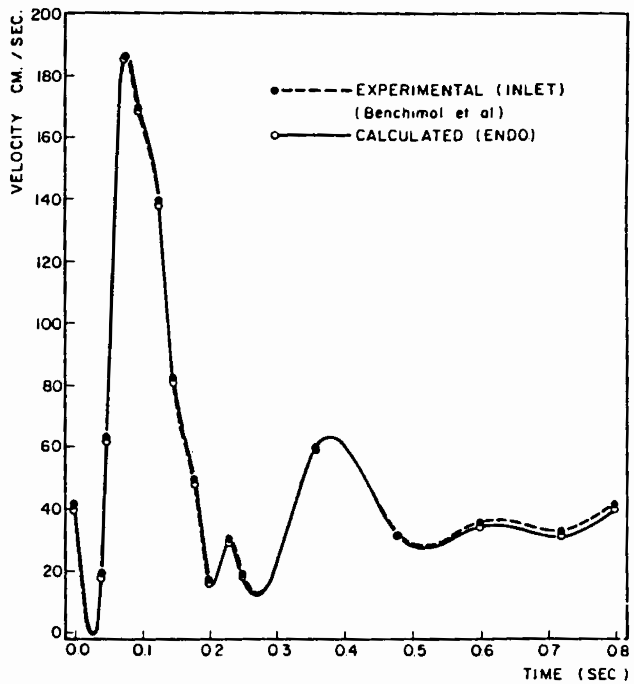

FIG. 2. Phasic velocity profiles, left ventricle: △ experimental (Benchimol et al.); □

The solution to Equations (35)–(36) yields

$$u^s = (\ln \eta_w)(x_1 - x) + x_1. \tag{37}$$

Note that u^s is also constrained at x_2, namely

$$u^s = x_2; \qquad x = x_2, \quad t \geqslant 0. \tag{38}$$

Thus, by Equations (2), (16), and (37)–(38), we can evaluate the phase difference ϕ between displacements of the endocardium and the epicardium interfaces:

$$\phi = \arcsin\left[\frac{-e^1\bar{\eta}_0 + \bar{x}_1 - \bar{x}_2}{\mathring{x}_2} + \frac{\mathring{x}_1}{\mathring{x}_2}\sin\omega t\right] - \omega t. \tag{39}$$

Again, neglecting the mass coupling coefficient and the body forces acting on the solid mass, and combining the solid and fluid equations of motion [Equations (46)–(47) in paper I], we have

$$\frac{\partial \sigma}{\partial x} = \gamma^F n_w \frac{\partial \psi_w}{\partial x} + \rho^s \frac{\partial^2}{\partial t^2}\left[(1 - n_w) u^s\right], \tag{40}$$

where ρ^s is the density of the solid.

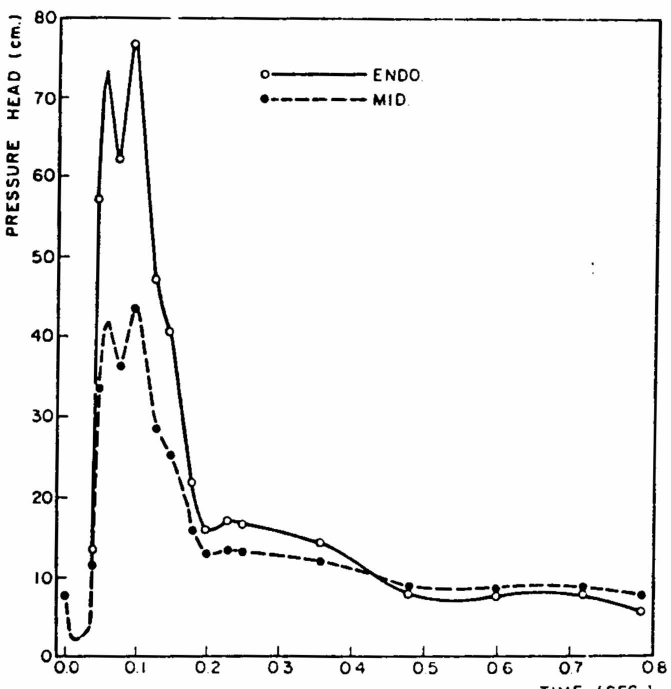

By Equations (31), (32), (35), and (37), Equation (40) can be rewritten as

$$\frac{\partial \sigma}{\partial x} = C_1 x + C_2, \tag{41}$$

where

$$C_1 = \gamma^F(1 - \eta_w)A_1 - \rho^s\left([1 + \ln \eta_w]\ddot{\eta}_w + \frac{\dot{\eta}_w^2}{\eta_w}\right), \tag{42.1}$$

$$C_2 = -\gamma^F(1 - \eta_w)A_2 + \rho^s\left([1 + \ln \eta_w](\ddot{\eta}_w x_1 + 2\dot{\eta}_w \ddot{x}_1 + \eta_w \ddot{x}_1) + \ddot{\eta}_w x_1 + \frac{\dot{\eta}_w^2 x_1}{\eta_w} + 2\dot{\eta}_w \dot{x}_1\right) \tag{42.2}$$

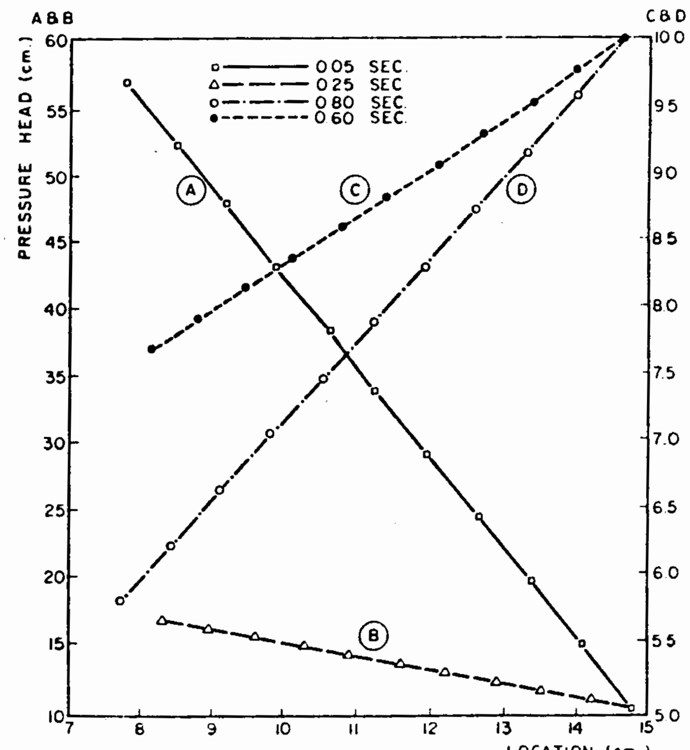

Equation (41) is to be solved for σ, subject to

$$\sigma = \sigma_2 \sin \omega t, \qquad x = x_2, \quad t \geq 0. \tag{43}$$

Thus, in view of Equations (41), (43), we obtain

$$\sigma = C_1 \frac{x^2 - x_2^2}{2} + C_2(x - x_2) + \sigma_2 \sin \omega t. \tag{44}$$

NUMERICAL EXAMPLE

The inflow and outflow phasic velocity profiles of Benchimol et al. [2–4] and Yamaguchi et al. [10] were used as input data for the LV cavity.

The mean displacements of the endocardium and epicardium were taken as 1.32 cm and 0.7 cm respectively, based on measurements of some 50

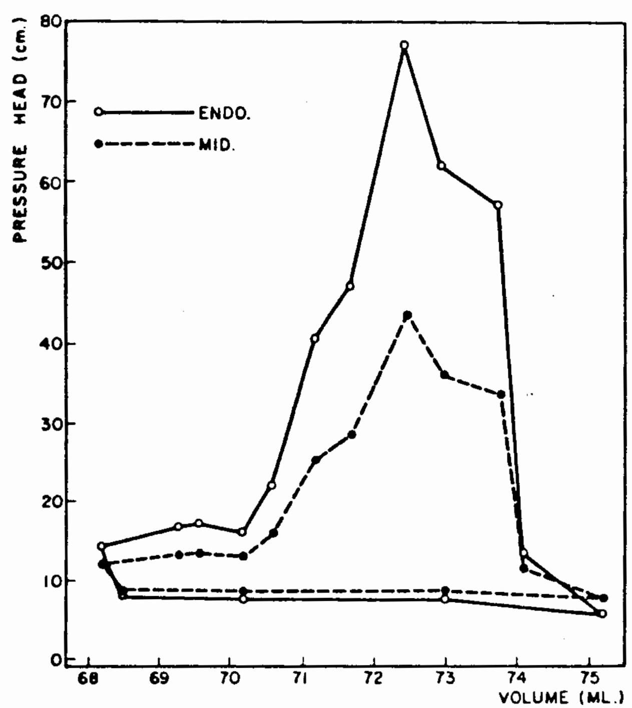

FIG. 5. Volume versus pressure head, left ventricle.

normal angiograms [7]. We took

$$\gamma = 0.0346 \text{ cm}^2/\text{sec}, \qquad \gamma^F = 1035 \text{ gf/cm}^3,$$
$$\rho^s = 1.06 \text{ g/cm}^3, \qquad \omega = \frac{2\pi}{0.8} \text{ Hz},$$
$$V_T = 158 \text{ cm}^3, \qquad V_{sB} = 3 \text{ cm}^3,$$
$$L = 14.8 \text{ cm}, \qquad V_{sw} = 3 \text{ cm}^3,$$
$$\psi_{B_L} = 10 \text{ cm}, \qquad \sigma_2 = 6.58 \text{ gf/cm}^2.$$

The numerical results are illustrated in Figures 2 to 8.

Figure 2 shows the phasic velocities in the cavity. The inlet velocity profile is based on measured data imposed as boundary condition, and the calculated profile at the endocardium is almost identical with the former.

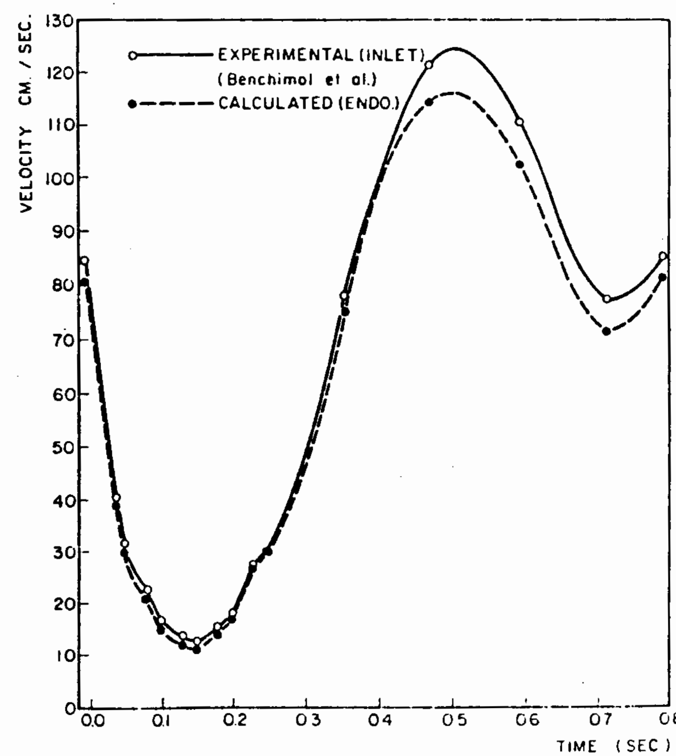

FIG. 6. Phasic velocity profiles, left-ventricle wall: △ experimental (Benchimol et al.); □ calculated.

(The slight differences are, however, rather important in the subsequent analysis of the pressure field.) The close similarity between the profiles is due to the insignificant effect of inertial terms in the assumed configuration.

Figure 3 shows the phasic blood pressure at the endocardium and at the mid point of the cavity. Note the double peak which corresponds to the inflection point in the velocity profiles in Figure 2. This phenomenon is associated with Equation (8), which relates the pressure gradient to the velocity.

Figure 4 shows the pressure distribution along the cavity at instants during the cardiac cycle. The prevalence of a pressure gradient in the cavity was also reported by Dinnar [6]. Curves A and B represent the pressure drop from the endocardium towards the valve during the systole, and curves C and D delineate the pressure gradient during the diastolic filling. The linearity of the graphs is attributable to the adopted one-dimensionality of the model.

Figure 5 shows closed pressure-head–volume loops of the cavity over a cycle. Note that less mechanical work (as evident from the smaller area of

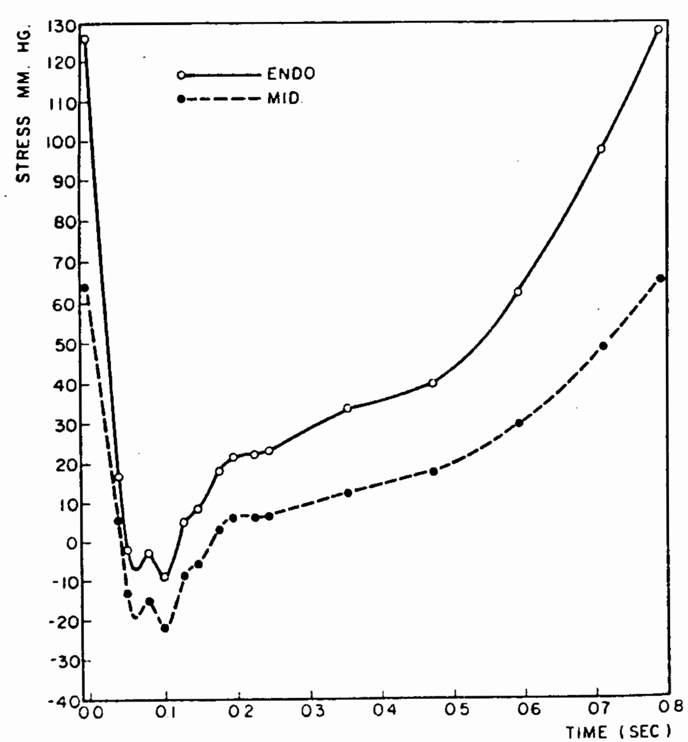

FIG. 7. Phasic stress profiles (fluid pressure + tissue stress), left ventricle wall

the loop) is done at the midpoint than on the endocardial side, the difference being due to the pressure gradient between the two points. Obviously, the authentic 3-D configuration, where internal turbulence may tend to reduce this apparent difference, should yield somewhat different results.

Figure 6 shows relative (fluid-solid) phasic velocity profiles inside the myocardium. The profile at the inlet (epicardial side) is based on measured experimental coronary data and is taken here as the boundary condition at the epicardium. The similarity between the epicardial and endocardial profiles is explained by the absence of inertial forces in the myocardial flow. Also, note that the myocardium is assumed here to be uniformly homogenous at each instant, with the porosity an explicit function of time alone. Accordingly, the instantaneous resistance is defined as constant across the wall.

Figure 7 shows the local profiles of the phasic stress due to the combined fluid pressure and stress inside the saturated solid matrix in the myocardium, during the cardiac cycle. Note the steep rise in compression during the

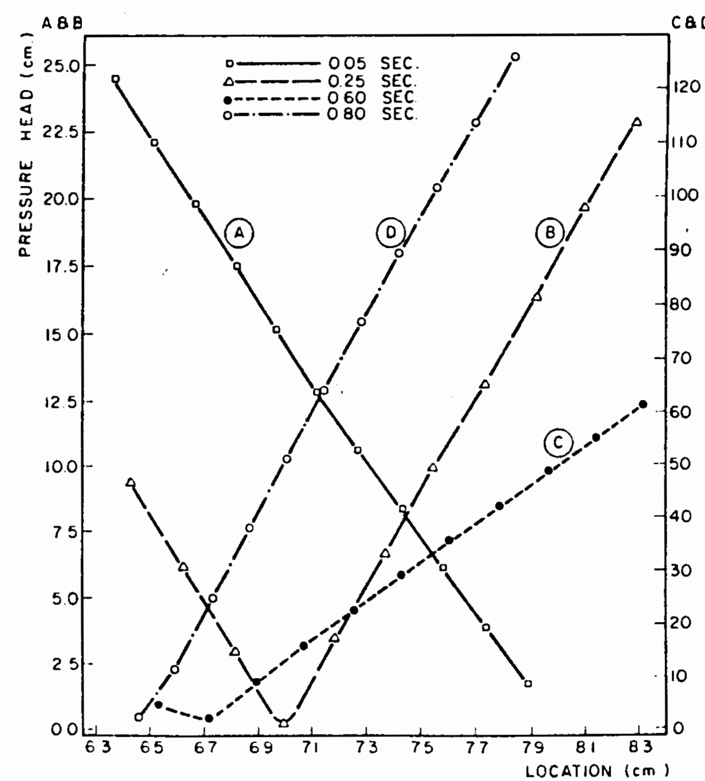

systole, consistent with earlier studies [1]. The double-peak configuration during the systole corresponds to the fluid pressure shown in Figure 3 and the boundary condition expressed in equation (30.1). The composite muscle then exhibits the development of tension during the diastole (corresponding to relief of stress when considereed in terms of absolute stress values).

Figure 8 shows the instantaneous combined stress distribution across the cavity wall over the cycle. Graph A represents the stress gradient during the systole. In the other graphs reversal of the slope from negative to positive indicates transition from compression to tension; thus, graph B represents the onset of the tension gradient in the epicardial layers during the systole, and graphs C and D represent the tension during the diastole. Note that the effect of the epicardial boundary compression, Equation (43), becomes minute towards the end of the diastole.

Figure 9 shows the distribution of mechanical work in the myocardium, again in the form of closed loops of combined stress versus volume. As

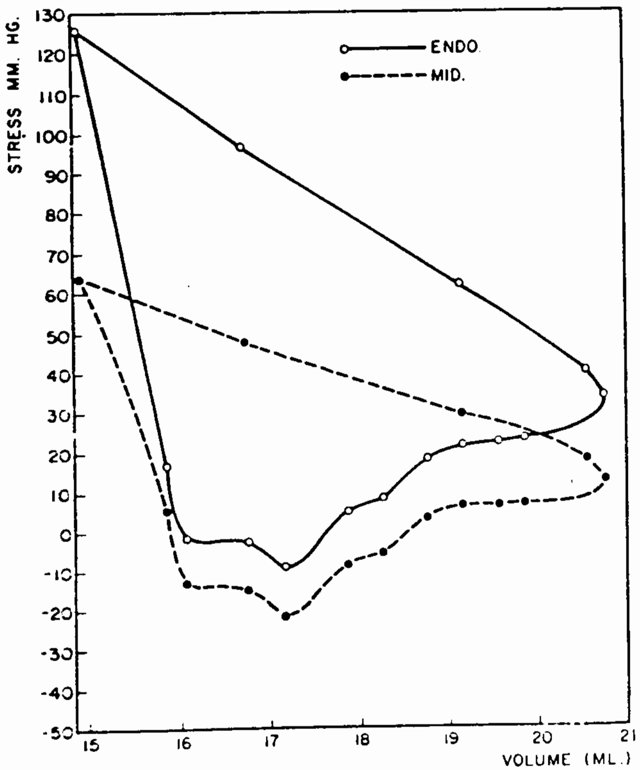

FIG. 9 Volume versus combined stress, left ventricle wall.

expected, the higher stress values at the endocardium result in more work being done there than at the midpoint.

The picture thus obtained demonstrates that in spite of the coarse time grid used, the model is capable of yielding meaningful results.

CONCLUSIONS

The efficacy of a porous-medium approach in assessing the heart mechanics is demonstrated by a 1-D approximation of the LV. Explicit functions for motion of the endocardium and epicardium obviate the need for constitutive laws, compatible relations, and iterative procedures. Application of material properties, such as permeability, porosity, and the phase difference between the displacement of the endocardium and epicardium, yields the pressure, stress, mechanical work, and velocity as functions of time and position. The simple 1-D approximation is consistent with experimental measurements of the phasic pressure and pressure versus volume in the LV. In the future, a worthwhile modification will consist in adjusting the endocardial displacement function to actual contraction and expansion measurements in the left ventricle. Implementation of the continuum theory [9] to develop a 2-D computer simulation is under way. This approach will yield, for example, the evolution of endocardial patterns subject to the different material and boundary conditions at the relevant sections.

SYMBOLS

This list contains symbols used in the companion paper [9] as well as this one.

LATIN

A, **B**, **C**	vectors of cosine directions and shape factors in the ventricles
A	area of tube's cross section
$\mathbf{b}^f, \mathbf{b}^s$	fluid and solids body forces respectively
C_B, C_w	Fluid specific capacity in the ventricles and myocardium respectively
g	acceleration of gravity
H	interface function
K	fluid permeability tensor in the myocardium
l	directional unit vector
L	tube length
n_B, n_w	effective porosity at the ventricles and myocardium respectively
n	unit vector normal to an interface, pointing outward
p_B, p_w	fluid pressure in the ventricles and myocardium respectively

q_B	fluid specific flux in the ventricles
Q_{B_Γ}	prescribed specific-flux value at the boundaries of the ventricles
$Q_{B2}, Q_{B1}, Q_{w2}, Q_{w1}$	outflow-inflow specific flux at tube's LV and myocardium boundaries respectively
$\mathbf{q}_w$	fluid-solid relative specific flux in the myocardium
$\mathbf{R}$	fluid resistance tensor in the myocardium
t	time
T_{ij}	stress tensor of the solid portion without fluid
$\mathbf{u}^s$	vector of average solid displacement
$\mathbf{v}_B$	fluid velocity vector in the ventricles
v^F, v^s	fluid and solid velocities respectively in the myocardium
V_w^F, V_w^s, V_w^b	volumes of fluid, solid, and the bulk in the myocardium
V_T, V_{TB}	total volume of tube and tube compartment respectively.
V_{Tw}, V_{Sw}	total and solid portion volumes at tube's myocardium
V_{sB}	volume of solid portion in the ventricles
$\mathbf{x}$	position vector (Cartesian coordinates)
x_1, x_2	prescribed displacements of tube's endocardium and epicardium
$\dot{\mathbf{x}}$	vector of interface (endocardium or epicardium) velocity
Z	nonlinear permeability in the ventricles
z	elevation spatial coordinate

GREEK

ρ^F, ρ^s	fluid and solid specific mass respectively
ψ_B, ψ_w	fluid pressure head in the ventricles and myocardium respectively
μ	fluid dynamic viscosity
τ	unit vector tangent to an interface
α_Γ	factor controlling the type of boundary condition
σ	stress of the solid-fluid mixture in the myocardium
ν	fluid kinematic viscosity, μ/ρ
ϕ	phase difference between tubes x_1 and x_2

SPECIAL

∇	gradient vector
$\frac{\partial}{\partial t}$	partial time derivative
$\frac{D}{Dt}$	hydrodynamic time derivative

$\Delta(\ )$	difference
$\frac{\mathscr{L}}{\mathscr{L}t}$	time-derivative operator [paper I, Equation (24)]
$[\ ]$	jump in a quantity

SUPERSCRIPTS AND DIACRITICALS

k	value already evaluated at present time
$k+1$	value to be evaluated at front time level
$*$	value attained by an iteration procedure
F	value associated with fluid portion
s	value associated with solid portion
b	value of the bulk volume in the myocardium
$\sim$	value from a previous evaluation

SUBSCRIPTS

Γ	value along boundary
B	value associated with the ventricles
w	value associated with the myocardium
ij	tensor components

This study was supported by a grant from the Kennedy-Leigh Fund and sponsored by the MEP Group, Women's Division, American Technion Society.

REFERENCES

1 R. Beyar and S. Sideman, Left ventricular mechanics related to the local distribution of oxygen demand through the wall, submitted for publication.

2 A. Benchimol and S. Matsuo, Continuous measurements of phasic aortic and coronary flow velocity during atrial fibrillation in man, Amer. J. Med. 51:466–473 (1971).

3 A. Benchiomol and K. B. Desser, Measurement of phasic aortocoronary bypass graft blood flow velocity in conscious man, *Amer. J. Cardiol.* 32:895–899 (1973).

4 A. Benchimol, K. B. Desser, and T. F. Wang, Doppler measurement of phasic continuous left ventricular blood flow velocity during ventricular arrhythmias, *Amer. Heart J.* 88(6):742–747 (1974).

5 J. H. U. Brown and D. S. Gann, *Engineering Principles in Physiology*, Vol. II, Academic, 1973.

6 U. Dinnar, Flow within the left ventricular cavity: Relative significance of various hemodynamics effects," in *Simulation and Imaging of the Cardiac System*, Martinus Nijhoff, 1985, pp. 232–243.

7 E. Marcus, E. Barta, R. Beyar, A. Battler, S. Rath, Y. Har-Zahav, D. Adam, and S. Sideman, Characterization of left ventricular contraction by a method of curvature difference analysis, submitted for publication.

8 J. T. Shepherd and P. M. Vanhouitte, *The Human Cardiovascular System*, Raven, 1980.

9 S. Sorek and S. Sideman, A porous-medium approach for modeling heart mechanics. I. Theory, *Math. Biosci.*

10 T. Yamaguchi et al., Measurement of turbulence intensity in the center of the canine ascending aorta with a hot-film anemometer, *J. Biomech. Engrg.* 105:177–187 (1983).

The Computational Complexity of Inferring Rooted Phylogenies by Parsimony*

WILLIAM H. E. DAY†
Centre de recherches mathématiques, Université de Montréal, Case Postale 6128, Succursale A, Montréal, Québec H3C 3J7, Canada

DAVID S. JOHNSON
AT&T Bell Laboratories 2C-355, 600 Mountain Avenue, Murray Hill, New Jersey 07974

AND

DAVID SANKOFF
Centre de recherches mathématiques, Université de Montréal, Case Postale 6128, Succursale A, Montréal, Québec H3C 3J7, Canada

Received 20 March 1986; accepted 11 April 1986

ABSTRACT

In systematics, parsimony methods construct phylogenies, or evolutionary trees, in which characters evolve with the least evolutionary change. The Camin-Sokal and Dollo parsimony criteria are used to construct phylogenies from discrete characters. Variations of these problems depend on whether characters are: cladistic (rooted) or qualitative (unrooted); binary (two states) or multistate (more than one state). The computational cost of known algorithms that guarantee optimal solutions to these problems increases exponentially with problem size; practical computational considerations restrict the use of such algorithms to analyzing problems of small size. We establish that the basic variants of these problems are all NP-complete and thus are so difficult computationally that efficient optimal algorithms are unlikely to exist for them.

1. INTRODUCTION

Systematists in recent years have witnessed a dramatic increase in the availability of computer resources for research. As a consequence, theoretical and practical investigations of numerical methods to infer phylogenies have

*The Natural Sciences and Engineering Research Council of Canada partially supported this research through individual operating grants to W. H. E. Day (A4142) and D. Sankoff (A8867), as well as through an infrastructure grant to D. Sankoff, R. J. Cedergren, and G. Lapalme (A3092).

†Permanent address: Department of Computer Science, Memorial University of Newfoundland, St. John's, NF A1C 5S7, Canada.

©Elsevier Science Publishing Co., Inc., 1986